Nano Research

Open Access

Research Article

Spatial confinement effect on hollow mesoporous carbon spheres/MOF-derived nanosheets superstructures for improved capacitive deionization performance

Yijian Tang[1], Shuai Cao[1], Wanchang Feng[1], Xiaotian Guo[1], Yangyang Sun[1], Songtao Zhang[1], Huaiguo Xue[1] ✉, and Huan Pang[1,2] ✉

[1] *School of Chemistry and Chemical Engineering, Yangzhou University, Yangzhou 225009, China*
[2] *State Key Laboratory of Coordination Chemistry, Nanjing University, Nanjing 210023, China*

Cite this article: *Nano Research*, **2025**, *18*, 94907194. https://doi.org/10.26599/NR.2025.94907194

ABSTRACT: Metal-organic framework (MOF) nanoparticles are successfully confined in the hollow mesoporous carbon spheres (HMCSs) through space-confined synthesis methods. The prepared ZIF-67@HMCSs nanocomposites act as effective sacrificial templates, which can afford Co^{2+} sources. After a facile solvothermal reaction and sequential cation etching, yolk–shell-structured layered double hydroxide@HMCSs (LDH@HMCSs) have been synthesized. The LDH@HMCSs nanocomposite possesses a three-dimensional (3D) hollow nanocage superstructure that effectively blocks the self-stacking of LDH nanosheets and promotes ion transport. Compared to CoFe-LDH@HMCSs, and Co-LDH@HMCSs, CoNi-LDH@HMCSs exhibit superior electrochemical performance and desalination performance due to the remarkable synergistic effect between the CoNi-LDH nanosheets and mesoporous N-doped carbon shells. The resultant CoNi-LDH@HMCSs-0.4-based capacitive deionization (CDI) device exhibits excellent salt adsorption capacity (SAC, 36.41 mg·g^{-1}) and good cycle stability. This work will confirm the significance of constructing superstructure and open new avenues for the practical application of CDI technology in water treatment.

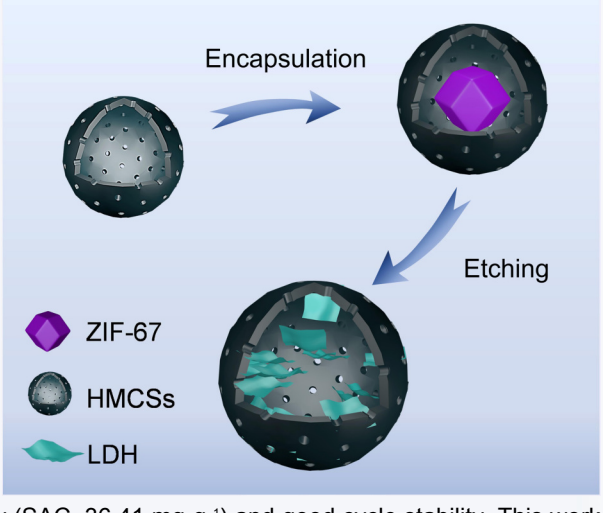

KEYWORDS: confined growth, hollow mesoporous carbon spheres, metal-organic framework (MOF)-derived layered double hydroxide, superstructure, capacitive deionization

1 Introduction

Constructing two-dimensional (2D) nanosheets into three-dimensional (3D) well-organized superstructures is one of the research hotspots in materials engineering and science [1–5]. The superstructures contain the basic units of various assemblies (e.g., nanoparticles, nanofibers, nanosheets, and nanocages), which typically exhibit excellent structural characteristics and attractive physicochemical performances [6]. Specifically, superstructures with controllable configuration, abundant mesopores, and high surface area exhibit excellent performance in a wide range of fields (energy, environment, sensors, adsorption, etc.) due to their enhanced mass transfer kinetics and numerous active sites [7–10]. Till now, the template method has been a common strategy used to construct superstructures [11]. Utilizing metal-organic framework (MOF) as a self-sacrificial template has been identified as a promising strategy for preparing 3D superstructures.

MOFs are a relatively new class of porous crystal materials formed by the coordination of metal ions and organic ligands [12–15]. The ion etching of MOFs is an effective method to produce morphologically controllable layered double hydroxides (LDHs) [16–18]. LDHs are classic 2D materials, which are considered as promising capacitive deionization (CDI) Faradic

Received: October 9, 2024; **Revised:** December 5, 2024
Accepted: December 16, 2024

✉Address correspondence to Huaiguo Xue, chhgxue@yzu.edu.cn; Huan Pang, huanpangchem@hotmail.com, panghuan@yzu.edu.cn

electrode materials due to their high specific surface area and ideal theoretical capacitance [19–21]. However, the inherent poor electrical conductivity and self-stacking characteristics of LDH with 2D structure result in suboptimal CDI properties. The spatial confinement synthesis of LDH nanosheets in hollow mesoporous carbon spheres (HMCSs) can effectively solve these issues. HMCSs, as one of the ideal nanoreactors, not only provide sufficient internal cavities as reaction sites, but also provide buffering space for the volume expansion of active substances [22–24]. Encapsulating nanoparticles into HMCSs is a classical design. This design is helpful to improve electrical conductivity and reduce mass transfer distance. Therefore, it can be believed that it makes sense to encapsulate MOF nanoparticles into HMCSs. More importantly, the presence of HMCSs facilitates the construction of MOF-derived 2D structured LDH nanosheets into HMCSs/LDH nanocomposites with 3D superstructures.

In this work, we successfully synthesized yolk–shell-structured ZIF-67@HMCS nanocomposites through a space-confined strategy, which uses HMCSs as the shell and ZIF-67 as the core. Therefore, the size of the ZIF-67 nanoparticles was well controlled. Then, the LDH@HMCSs (CoNi-LDH@HMCSs, CoFe-LDH@HMCSs, and Co-LDH@HMCSs) superstructures have been prepared by metal ions (Fe^{3+}, Co^{2+}, and Ni^{2+}) etching of ZIF-67@HMCS templates. The LDH@HMCSs with 3D hollow nanocage superstructures not only suppress the self-stacking of LDH, but also facilitate ion transportation. The CoNi-LDH@HMCSs electrode displayed higher electrochemical and CDI performance than Co-LDH@HMCSs, and CoFe-LDH@HMCSs due to the remarkable synergistic effect between the CoNi-LDH nanosheets and mesoporous N-doped carbon shells. In addition, the nickel ion content was regulated during the ion etching process, and the CoNi-LDH@HMCSs-0.4 electrode shows the optimal electrochemical performance due to its high specific surface area and more defects. The CoNi-LDH@HMCSs-0.4 electrode displayed a high salt adsorption capacity (SAC) of 36.41 $mg \cdot g^{-1}$ and exceptional cycle stability. More significantly, the mechanism of ion adsorption and transport kinetics in CoNi-LDH@HMCSs was explained using *ex situ* X-ray diffraction (XRD) analysis and theoretical models, and the role of LDH in composite materials was revealed via density functional theory (DFT).

2 Results and discussion

The process of synthesizing yolk–shell-structured LDH@HMCSs is schematically shown in Fig. 1. HMCSs (Fig. S1 in the Electronic Supplementary Material (ESM)) with a cavity diameter of about 250 nm were prepared from the previously reported synthesis method [25]. The carbon shell thickness of HMCSs is about 10 nm. The cavity of HMCSs was used as a nanoreactor to spatially confine the formation of ZIF-67 and their derivatives (LDH), and the yolk–shell structure was obtained.

ZIF-67 was synthesized by self-assembly of Co^{2+} and 2-methylimidazole (2-MeIm) in a cavity of HMCSs under stirring at low temperature, and yolk–shell-structured ZIF-67@HMCSs (Fig. S2 in the ESM) were then prepared. As shown in the XRD patterns (Fig. S3 in the ESM), all the diffraction peaks of ZIF-67@HMCSs are consistent with the characteristic peaks of ZIF-67. Afterwards, ZIF-67@HMCSs were transformed into the corresponding LDH@HMCSs (CoFe-LDH@HMCSs, Co-LDH@HMCSs, and CoNi-LDH@HMCSs) by metal ions (Fe^{3+}, Co^{2+}, and Ni^{2+}) etching. In this process, the protons generated by metal ions (Fe^{3+}, Co^{2+}, and Ni^{2+}) hydrolysis will enter the ZIF-67 framework, interrupting the coordination of Co^{2+} with 2-MeIm. The released portion of Co^{2+} ions is oxidized to Co^{3+} ions in the mixed solution by dissolved oxygen and nitrate anions [26]. Subsequently, Co^{2+}/Co^{3+} in the mixed solution couples with metal ions (Fe^{3+}, Co^{2+}, and Ni^{2+}) and OH^- to form LDH within the cavity of HMCSs. Eventually, the ZIF-67 template decomposes in the inner cavity of the HMCSs, forming a yolk–shell-structured LDH@HMCSs. For comparison, a similar method was used to prepare a 2D structured LDH (Figs. S5–S7 in the ESM) using ZIF-67 (Fig. S4 in the ESM) as a sacrificial template. The (003), (006), (009), and (110) crystal planes of CoFe-LDH, Co-LDH, and CoNi-LDH shown in the XRD patterns (Figs. S8–S10 in the ESM) represent the characteristic peaks of typical LDH phase [27].

The morphology of LDH@HMCSs can be obviously observed by scanning electron microscopy (SEM) and transmission electron microscopy (TEM) images. Figures 2(a)–2(c) show that Co-LDH nanosheets grow very little in the interior of HMCSs. The energy dispersive spectroscopy (EDS) element mapping images (Fig. 2(d)) indicate that the signal of Co element matches well with Co-LDH nanosheets, with C and N elements exhibiting extremely strong signals at the carbon shell, while O element is distributed on the LDH nanosheets and carbon shell. The XRD pattern for Co-LDH@HMCSs (Fig. 2(e)) shows four peaks at 11.58, 22.74, 33.48, and 59.74°, corresponding to the (003), (006), (009), and (110) planes of the LDH phase (PDF#46-0605) [28]. SEM and TEM images (Figs. 2(f)–2(h)) of CoFe-LDH@HMCSs show that CoFe-LDH nanosheets densely grow inside HMCSs and diffuse to the surface of the carbon shell. Figure 2(i) shows that the distribution of C, O, N, Co elements in CoFe-LDH@HMCSs is the same as that of Co-LDH@HMCSs. In addition, Fe element is well distributed on CoFe-LDH nanosheets. The characteristic peaks of the CoFe-LDH@HMCSs in XRD pattern (Fig. 2(j)) are also consistent with the LDH phase (PDF#50-0235) [29]. As shown in Figs. 2(k)–2(m) and Figs. S11 and S12 in the ESM, CoNi-LDH nanosheets grow densely in the interior of HMCSs. CoNi-LDH nanosheets exhibit relatively small and thin characteristics. The EDS element mapping images of CoNi-LDH@HMCSs (Fig. 2(n)) show that the distribution of C, O, N, Co elements in CoNi-LDH@HMCSs is the same as that of Co-LDH@HMCSs. Ni element is well distributed on CoNi-LDH nanosheets. The XRD patterns of CoNi-LDH@HMCSs (Fig. 2(o)) show (002) plane of the amorphous carbon frameworks and (003), (006), (012), and (110) planes of the

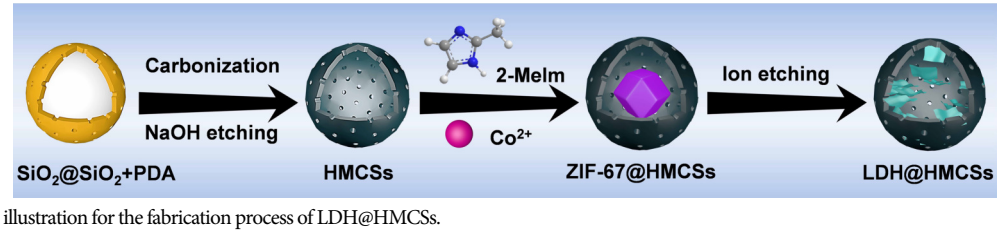

Figure 1 Schematic illustration for the fabrication process of LDH@HMCSs.

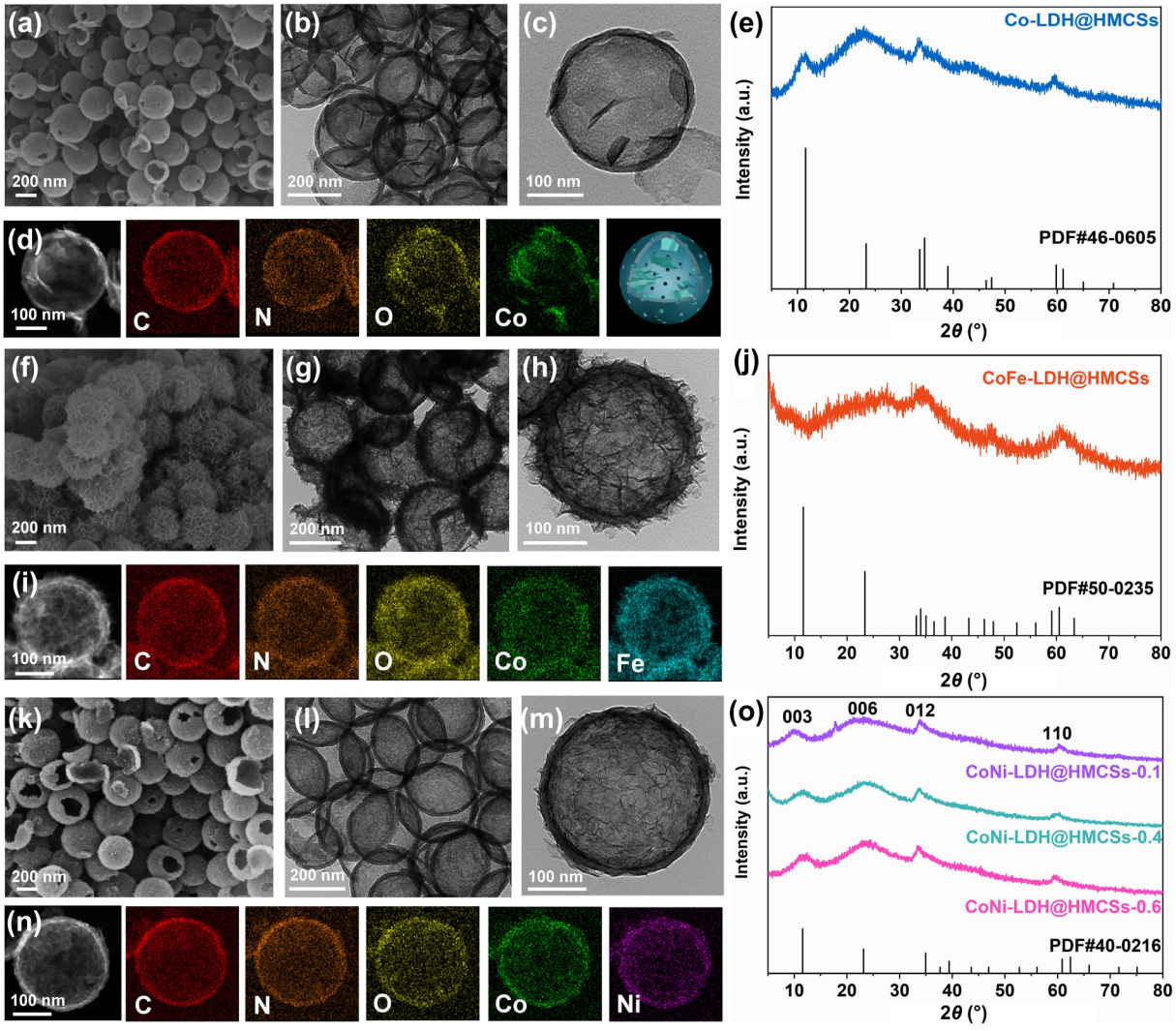

Figure 2 (a) SEM, (b) and (c)TEM, (d) EDS element mapping images, and (e) the corresponding XRD pattern of Co-LDH@HMCSs. (f) SEM, (g) and (h) TEM, and (i) EDS element mapping images, and (j) the corresponding XRD pattern of CoFe-LDH@HMCSs. (k) SEM, (l) and (m) TEM, and (n) the corresponding EDS element mapping images of CoNi-LDH@HMCSs-0.4. (o) XRD patterns of CoNi-LDH@HMCSs.

LDH phase (PDF#40-0216) [30]. Moreover, the doping content of Ni ions has little effect on the crystal planes of CoNi-LDH@HMCSs. From the above analysis, it could be well proved that ZIF-67@HMCSs were successfully converted into LDH@HMCSs.

The structures of HMCSs, CoFe-LDH@HMCSs, Co-LDH@HMCSs, and CoNi-LDH@HMCSs were further explored by Raman spectrum. Two broad peaks at ≈ 1350 and 1585 cm^{-1} could be seen (Fig. 3(a) and Fig. S13 in the ESM) in HMCSs and LDH@HMCSs, attributed to the D and G bands, respectively. The intensity ratio (I_D/I_G) between the D-band and G-band is commonly used to reflect the degree of disorder and the number of defects [31–33]. The I_D/I_G values of HMCSs, CoFe-LDH@HMCSs, Co-LDH@HMCSs, and CoNi-LDH@HMCSs are 0.878, 0.905, 0.906, and 0.927, respectively. Remarkably, the introduction of LDH leads to an increase in I_D/I_G compared to HMCSs. In the synthetic process of CoNi-LDH@HMCSs, the content of nickel nitrate introduced also has a certain influence on the I_D/I_G value. The ratio for CoNi-LDH@HMCSs-0.4 (I_D/I_G = 0.927) is higher than that for CoNi-LDH@HMCSs-0.1 (I_D/I_G = 0.886) and CoNi-LDH@HMCSs-0.6 (I_D/I_G = 0.898). This implies that CoNi-LDH@HMCSs-0.4 possesses the highest degree of disorder and the most defects, which promote the ability to charge accumulation [31].

The pore structure of the as-prepared materials has been characterized by N_2 adsorption–desorption isotherm. N_2 adsorption–desorption isotherms for all LDH@HMCSs and HMCSs samples (Fig. 3(b) and Figs. S15(a) and S15(c) in the ESM) suggest the presence of mesopores (type IV) [34]. The hysteresis loops of P/P_0 in the range of 0.5 to 1.0 are caused by the presence of mesopores [35, 36]. The hysteresis loops of CoNi-LDH@HMCSs, CoFe-LDH@HMCSs, and Co-LDH@HMCSs are significantly smaller than that of HMCSs, which fully proves that LDH nanosheets occupy the cavity of HMCSs. The pore size distribution was analyzed by the BJH method and the results were shown in Fig. 3(c) and Figs. S14(b), S14(d), S15(b), and S15(d) in the ESM. The pore size distributions of all LDH@HMCSs and HMCSs materials exhibit pore size centered at ≈ 2.7 nm, confirming the existence of mesoporous structure, which provides a low resistance channel for ions and is conducive to ion diffusion [37]. The specific surface area (SSA) and pore size parameters of all as-prepared materials are presented in Table S1 in the ESM. The SSA of CoNi-LDH@HMCSs-

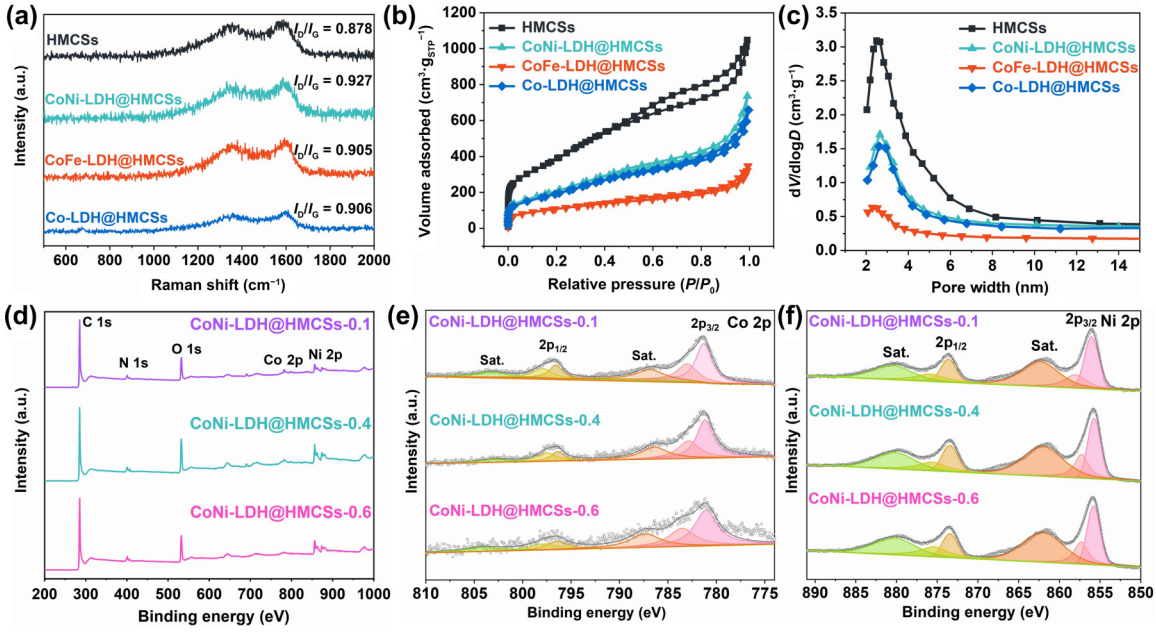

Figure 3 (a) Raman spectra, (b) N_2 adsorption–desorption isotherms, (c) BJH pore size distribution of HMCSs, CoNi-LDH@HMCSs, CoFe-LDH@HMCSs, and Co-LDH@HMCSs samples. (d) XPS survey spectra and high-resolution (e) Co 2p and (f) Ni 2p spectra of CoNi-LDH@HMCSs-0.1, CoNi-LDH@HMCSs-0.4, and CoNi-LDH@HMCSs-0.6 samples.

0.4 (774.4 $m^2 \cdot g^{-1}$) is larger than that of Co-LDH@HMCSs (717.5 $m^2 \cdot g^{-1}$), and CoFe-LDH@HMCSs (391.6 $m^2 \cdot g^{-1}$), but smaller than that of original HMCSs (1458.1 $m^2 \cdot g^{-1}$). These results indicate that the formation of LDH makes the original HMSCs lose their unique hollow structure, and the formation of random orientation promotes the formation of a yolk–shell structure. Moreover, the SSA of CoNi-LDH@HMCSs-0.4 (774.4 $m^2 \cdot g^{-1}$) is higher than that of CoNi-LDH@HMCSs-0.1 (740.7 $m^2 \cdot g^{-1}$) and CoNi-LDH@HMCSs-0.6 (758.3 $m^2 g^{-1}$).

The elemental compositions and valence states of the prepared LDH@HMCSs were explored by X-ray photoelectron spectroscopy (XPS) analytical method (Figs. 3(d)–3(f) and Figs. S16–S19 in the ESM). XPS measurements (Fig. 3(d)) further confirm the presence of C, N, O, Ni, and Co elements in the CoNi-LDH@HMCSs samples. The C 1s (Fig. S16 in the ESM) peaks at approximately 284.8, 285.3, 286.7, and 289.3 eV can be attributed to HMCSs in the form of C–C, C–N, C–O, and O–C=O, respectively [38]. The O 1s spectra are fitted into three peaks corresponding to the oxygen of water, –OH bonds, and metal (Ni and Co)–O bonds (Fig. S17 in the ESM) [39]. The Co 2p spectra (Fig. 3(e)) contain two sets of double peaks designated as Co^{2+} (782.9 and 797.5 eV) and Co^{3+} (781.2 and 796.4 eV), clarifying the partial oxidation of Co [40]. The XPS spectra of Ni 2p (Fig. 3(f)) indicate the existence of Ni^{2+} (855.8 and 873.5 eV) and Ni^{3+} (857.3 and 875.7 eV) [41]. These results further prove the formation of NiCo-based LDH structure. In addition, the formation of LDH is also conducive to enhancing the hydrophilicity of the material [39]. The contact angle measurements shown in Fig. S20 in the ESM further prove that the solid–liquid contact angle of LDH@HMCSs composite is significantly smaller than that of pure HMCSs, indicating that LDH@HMCSs composite shows better hydrophilicity. The good wettability can reduce the solid–liquid interfacial tension around the nanopore, thus making it easier for aqueous solution to enter the nanopore [9]. Therefore, combining LDH nanosheets with HMCSs to obtain a better chemical composition is a necessary condition for obtaining good CDI properties.

To evaluate the electrochemical performance of electrodes, a three-electrode system was studied under 1.0 M NaCl solution. The galvanostatic charge–discharge (GCD) curves of HMCSs, CoNi-LDH, CoNi-LDH@HMCSs, CoFe-LDH@HMCSs, and Co-LDH@HMCSs samples shown in Fig. 4(a) and Figs. S21(a), S21(b), S22(a)–S22(c), and S23(a)–S23(c) in the ESM display slightly distorted triangles due to the presence of pseudocapacitive behavior. Moreover, the CoNi-LDH@HMCSs electrode at 0.5 $A \cdot g^{-1}$ (Fig. 4(a)) displays the longest discharge time, revealing that its GCD specific capacitance is also larger than other electrodes. It can also be seen from Fig. S24(a) in the ESM that the discharge time of CoNi-LDH@HMCSs-0.4 is longer than that of CoNi-LDH@HMCSs-0.1 and CoNi-LDH@HMCSs-0.6. The cyclic voltammetry (CV) curves of HMCSs, CoNi-LDH, CoFe-LDH@HMCSs, Co-LDH@HMCSs, and CoNi-LDH@HMCSs samples (Fig. 4(b) and Figs. S21(c), S21(d), S22(d)–S22(f), and S23(d)–S23(f) in the ESM) show the slightly distorted rectangular shapes without obvious redox peaks, indicating pseudocapacitive behaviour [42]. Figure 4(b) shows that the area enclosed by CoNi-LDH@HMCSs electrode is also significantly larger than that of other electrode materials, revealing that CoNi-LDH@HMCSs show the highest specific capacitance. The corresponding specific capacitances ($F \cdot g^{-1}$) at 5 $mV \cdot s^{-1}$ are as follows: CoNi-LDH@HMCSs (177.2) > Co-LDH@HMCSs (174.6) > CoFe-LDH@HMCSs (123.5) > HMCSs (108.4) > CoNi-LDH (30.9). Moreover, the area enclosed by CoNi-LDH@HMCSs-0.4 electrode (Fig. S24(b) in the ESM) is also significantly larger than that of CoNi-LDH@HMCSs-0.1 and CoNi-LDH@HMCSs-0.6. These results indicate that the formation of CoNi-LDH is more favorable to the electrochemical properties of LDH@HMCS composites than CoFe-LDH and Co-LDH. Moreover, the CoNi-LDH@HMCSs-0.4 electrode shows the highest specific capacitance (Table S2 in the ESM). Figure 4(c) shows the correlation between capacitance and scan rate for HMCSs, CoNi-LDH, CoNi-LDH@HMCSs, CoFe-LDH@HMCSs, and Co-LDH@HMCSs. At low scanning rates, ions have enough time to diffuse into the pores to form an electric double layer [43], and the presence of LDH

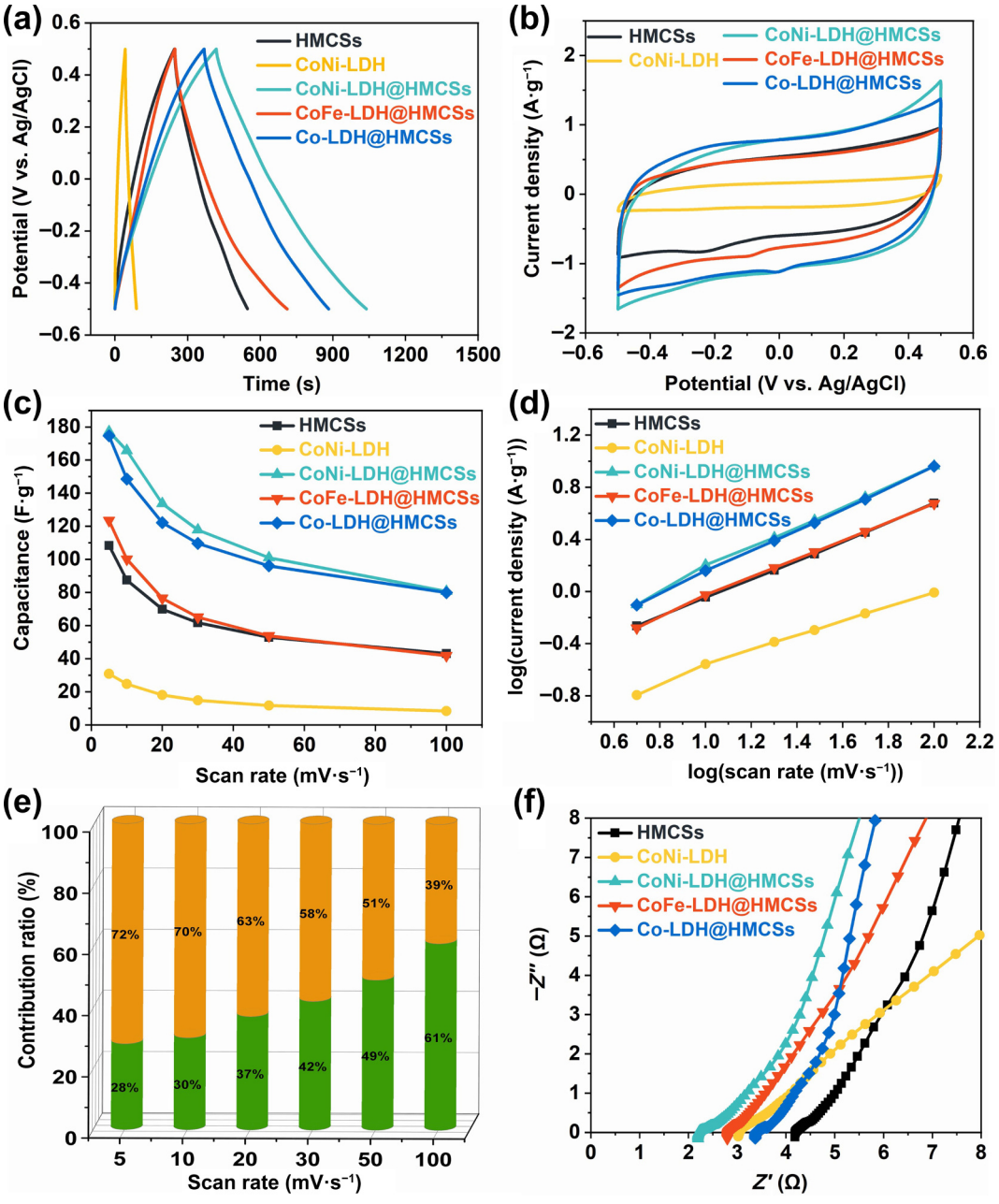

Figure 4 (a) GCD diagrams at 0.5 A·g^{-1}, (b) CV diagrams at 5 mV s^{-1}, (c) the specific capacitance vs. scan rate, (d) the fitted log plots of current density and scan rate, and (f) Nyquist plots of HMCSs, CoNi-LDH, CoNi-LDH@HMCSs, CoFe-LDH@HMCSs, and Co-LDH@HMCSs electrodes. (e) Capacitive ratio of CoNi-LDH@HMCSs electrode materials at different scan rates.

increases pseudocapacitance. On the contrary, at higher scanning rates, this trend is bound to weaken.

To explore the electrochemical kinetic properties of HMCSs, CoNi-LDH, and LDH@HMCSs electrodes, diffusion control and capacitive behavior were analyzed in detail. Figure 4(d) shows that the *b* values of the HMCSs, CoNi-LDH, CoNi-LDH@HMCSs, CoFe-LDH@HMCSs, and Co-LDH@HMCSs samples are 0.72, 0.59, 0.80, 0.73, and 0.81, respectively, indicating that the CoNi-LDH@HMCSs electrode is mainly affected by capacitive-controlled behavior [44]. As shown in Fig. 4(e) and Fig. S25 in the ESM, the capacitive contribution of the CoNi-LDH@HMCSs electrode is increased from 28% to 61% with the increase of the scan rates. Notably, the CoNi-LDH@HMCSs material with high specific capacitance can promote fast and reversible ion storage. The charge and ion transport kinetics of the HMCSs, CoNi-LDH, CoNi-LDH@HMCSs, CoFe-LDH@HMCSs, and Co-LDH@HMCSs electrodes were also investigated by electrochemical impedance spectroscopy (EIS, Fig. 4(f)). The Nyquist diagram in low-frequency region shows that the CoNi-LDH@HMCSs electrode possesses a steeper gradient and a larger slope than other electrodes. Moreover, the high-frequency region of Nyquist diagram illustrates the smallest *x* intercept for CoNi-LDH@HMCSs electrode [45]. In short, the CoNi-LDH@HMCSs electrode apparently possesses the best electrical conductivity and the fastest ion diffusion rate, which is also beneficial for ion storage and adsorption.

The SAC of all electrodes was systematically explored by assembling membrane-assisted CDI (MCDI) cells (Fig. 5(a)). The SAC of HMCSs, CoNi-LDH, CoNi-LDH@HMCSs, CoFe-

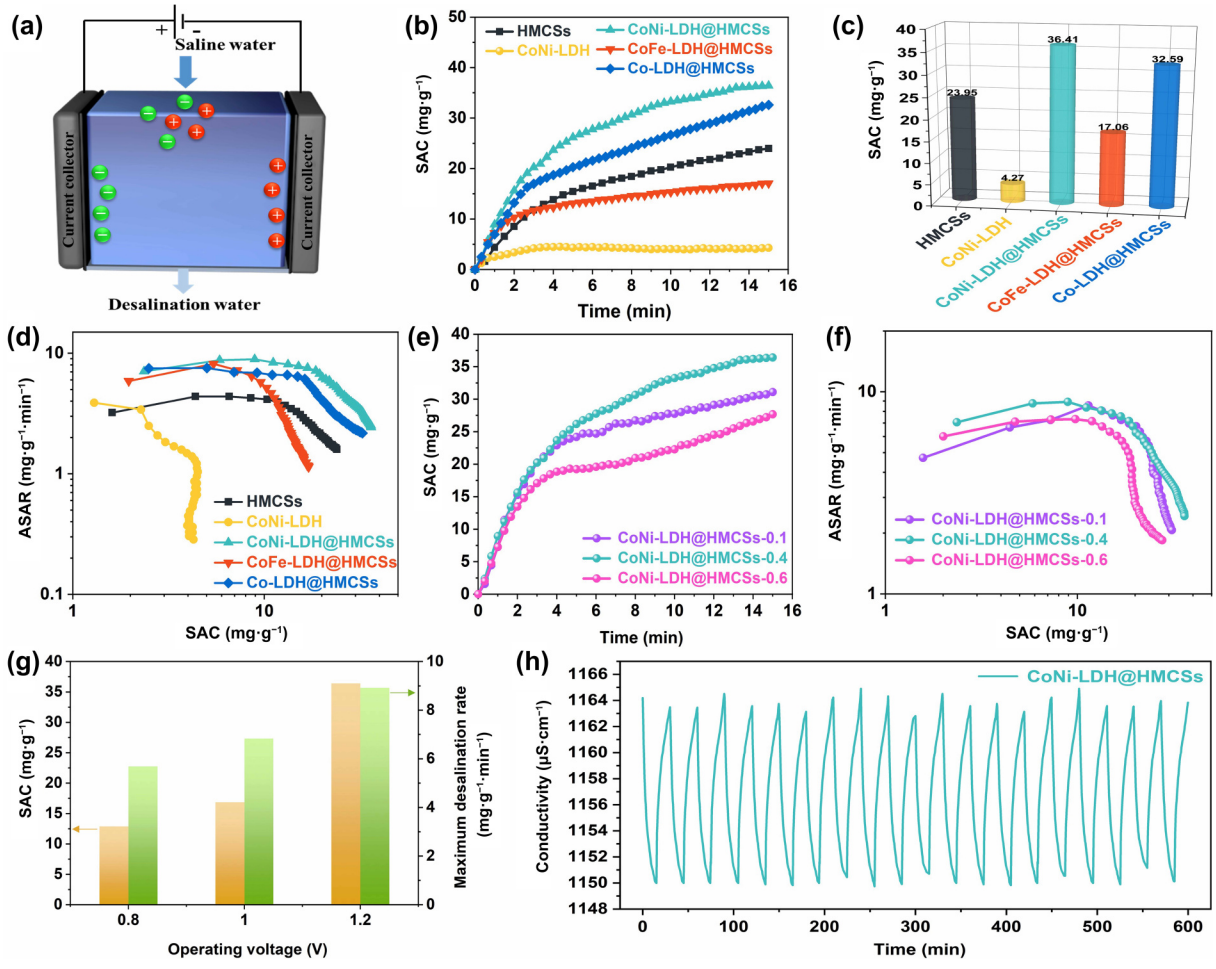

Figure 5 (a) Schematic diagram of CDI. (b) SAC-time plots, (c) desalination capacities, (d) CDI Ragone plots of HMCSs, CoNi-LDH, CoNi-LDH@HMCSs, CoFe-LDH@HMCSs, and Co-LDH@HMCSs electrodes. (e) SAC-time plots and (f) CDI Ragone plots of CoNi-LDH@HMCSs-0.1, CoNi-LDH@HMCSs-0.4, and CoNi-LDH@HMCSs-0.6 electrodes. (g) SAC values and maximum desalination rate of CoNi-LDH@HMCSs-0.4 at different operating voltages. (h) Cycle stability of CoNi-LDH@HMCSs-0.4 electrode in 10.0 mM NaCl solution.

LDH@HMCSs, and Co-LDH@HMCSs electrodes were explored in 10.0 mM NaCl at 1.2 V. It can be clearly observed from SAC-time plots (Fig. 5(b)) that the upward trend of CoNi-LDH@HMCSs electrode is faster than that of HMCSs, CoNi-LDH, CoFe-LDH@HMCSs, and Co-LDH@HMCSs electrodes within 15 min. The corresponding SAC values ($mg·g^{-1}$) are as follows (Fig. 5(c)): CoNi-LDH@HMCSs (36.41) > Co-LDH@HMCSs (32.59) > HMCSs (23.95) > CoFe-LDH@HMCSs (17.06) > CoNi-LDH (4.27), which indicates that the combination of CoNi-LDH and HMCSs is more conducive to the improvement of CDI characteristics. The CDI Ragone plots of these five electrodes are shown in Fig. 5(d). It is well known that the trend of moving up and right in these plots implies high electro-sorption performance and rate [46–48]. Apparently, CoNi-LDH@HMCSs electrode displays the most effective adsorption efficiency during CDI process. In order to better explore the effect of nickel contents on CDI performance, we further tested CoNi-LDH@HMCSs electrodes with different nickel contents. The SAC-time diagrams (Fig. 5(e)) of the CoNi-LDH@HMCSs-0.1, CoNi-LDH@HMCSs-0.4, and CoNi-LDH@HMCSs-0.6 electrodes show the fastest upward trend of CoNi-LDH@HMCSs-0.4. The SAC of CoNi-LDH@HMCSs-0.4 (36.41 $mg·g^{-1}$) can be calculated by Eq. (S7) in the ESM, which is higher than that of CoNi-LDH@HMCSs-0.1 (31.08 $mg·g^{-1}$), and CoNi-LDH@HMCSs-0.6 (27.67 $mg·g^{-1}$). Compared with the CDI performance of other similar carbon-based materials (Table S3 in the ESM), the CoNi-LDH@HMCSs-0.4 electrode also performs well. Moreover, it can be observed from the CDI Ragone diagram (Fig. 5(f)) that the CoNi-LDH@HMCSs-0.4 electrode shows the highest desalination capacity and rate. The desalination performance of the CoNi-LDH@HMCSs-0.4 electrode at different operating voltages (0.8–1.2 V) has also been evaluated. It is evident that as the voltage increases, the SAC value and maximum desalination rate are both increasing (Fig. 5(g)). Eventually, the cycle stability for the desalination/regeneration property of CoNi-LDH@HMCSs-0.4 electrode was also investigated. Figure 5(h) illustrates that the CoNi-LDH@HMCSs-0.4 electrode shows no significant degradation after 20 salt adsorption–desorption cycles, indicating its good cycling performance.

To further understand the mechanisms of ion adsorption and transport kinetics in CoNi-LDH@HMCSs, we developed *ex situ* XRD analysis and sophisticated theoretical models. The two XRD diffraction peaks (Fig. 6(a)) associated with Cl^- insertion at 31.4° and 45.1° intensify sharply at charge and then disappear completely after discharge, indicating the reversible Cl^- capture capability of CoNi-LDH@HMCSs during electrochemical processes [39].

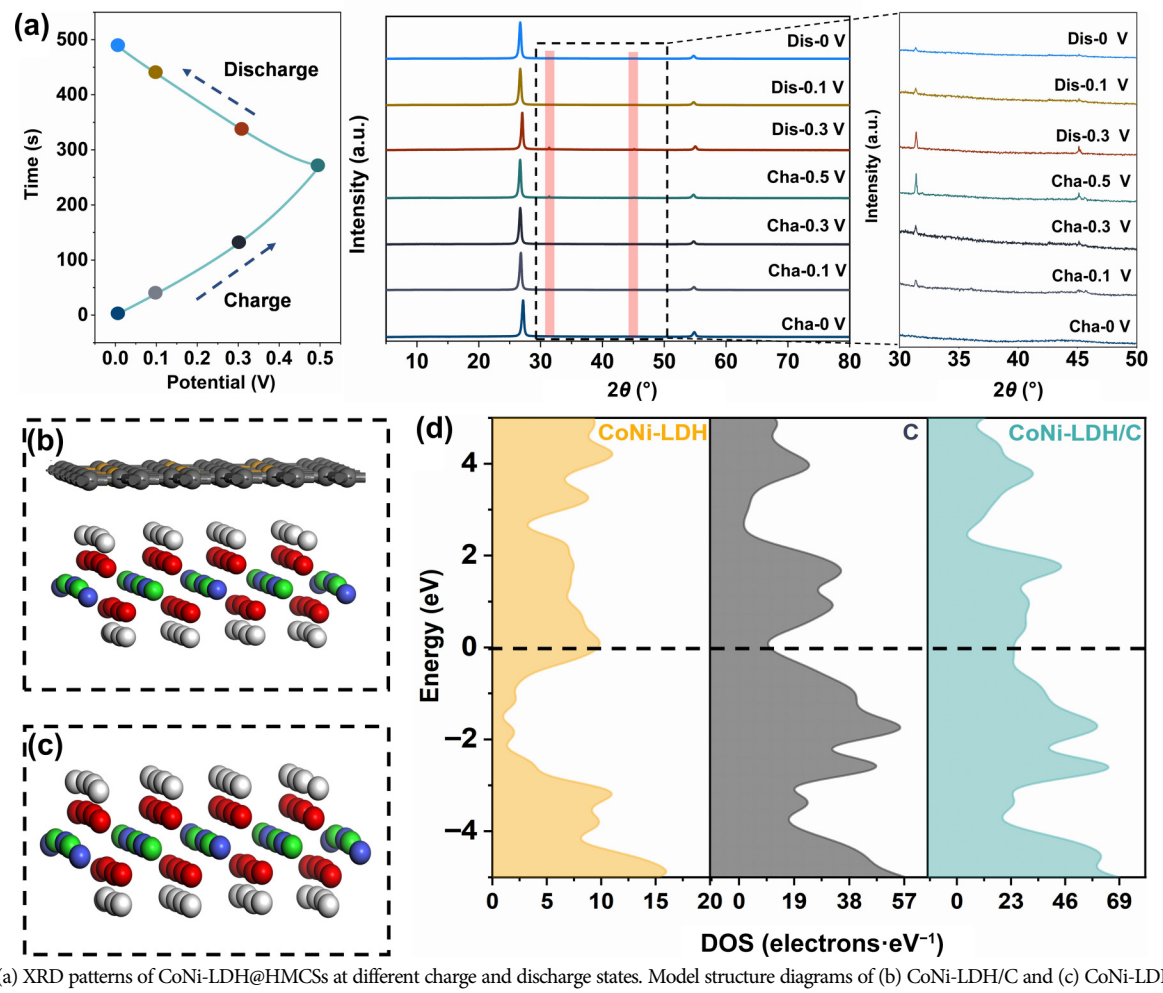

Figure 6 (a) XRD patterns of CoNi-LDH@HMCSs at different charge and discharge states. Model structure diagrams of (b) CoNi-LDH/C and (c) CoNi-LDH based on DOS calculations (blue: Co, green: Ni, red: O, white: H, black: C, and yellow: N). (d) The DOS diagrams of CoNi-LDH, C, and CoNi-LDH/C.

Figures 6(b) and 6(c) present the model structure derived from density of states (DOS) curve calculations, establishing a theoretical framework for analyzing the electronic structure characteristics of the material. A comparative analysis of DOS curves for CoNi-LDH, C, and CoNi-LDH/C materials is presented in Fig. 6(d). The results reveal that the optimized CoNi-LDH/C composite exhibits a higher density of electronic states near the Fermi level than that of the C and CoNi-LDH materials, indicative of significantly enhanced metal-adsorbate interactions in CoNi-LDH/C composite [49]. This further indicates that the synergistic effect between CoNi-LDH and C is beneficial for enhancing electrical conductivity and electron transfer. This observation is consistent with the above experimental conclusions. Therefore, the combination of carbon and LDH material can well enhance the conductivity of the composite. This achievement not only underscores the innovative aspects of our material design and preparation but also opens new avenues for the practical application of CDI technology in water treatment processes.

The yolk–shell-structured LDH@HMCSs show excellent electrochemical properties as a CDI electrode material, mainly due to the following aspects: (1) The pore structure of LDH@HMCSs enables the salt solution to penetrate into HMCSs effectively, providing a large contact area for ion adsorption. (2) The core of LDH nanosheets can effectively improve the wettability of the composite, make the aqueous solution more easily enter the nanopore, and promote the ion adsorption. (3) The shell of mesoporous carbon as a conductive matrix significantly improves the electrical conductivity of the composite. (4) The yolk–shell superstructure provides enough buffer space for LDH nanosheets to adsorb ions, preventing the agglomeration of the LDH nanosheets in the CDI process.

3 Conclusions

In summary, yolk–shell-structured LDH@HMCSs were synthesized through simple ion etching of ZIF-67@HMCSs template. HMCSs not only provide space for confined growth of ZIF-67, but also serve as conductive networks to enhance the conductivity of LDH@HMCSs. The CoNi-LDH@HMCSs electrode shows higher CDI performance than Co-LDH@HMCSs, and CoFe-LDH@HMCSs, which is attributed to the remarkable synergistic effect between the CoNi-LDH nanosheets and mesoporous N-doped carbon shells. The CoNi-LDH@HMCSs electrode shows a high SAC of 36.41 $mg \cdot g^{-1}$ in an initial 10.0 mM NaCl solution, which outperforms the primary CoNi-LDH electrode (4.27 $mg \cdot g^{-1}$) and HMCSs electrode (23.95 $mg \cdot g^{-1}$). The DFT results further demonstrate that the synergistic effect between CoNi-LDH and C is beneficial for enhancing electrical conductivity and electron transfer. This work will provide solid guidance for the confined growth of 2D nanosheets in HMCSs, further confirming the significance of constructing superstructure.

Electronic Supplementary Material: Supplementary material (electrochemical measurements, XRD, and XPS) is available in the online version of this article at https://doi.org/10.26599/NR.2025.94907194.

Data availability

All data needed to support the conclusions in the paper are presented in the manuscript and the Electronic Supplementary Material. Additional data related to this paper may be requested from the corresponding author upon request.

Acknowledgements

This work was supported by the National Natural Science Foundation of China (No. 52371240).

Declaration of competing interest

All the contributing authors report no conflict of interests in this work.

Author contribution statement

Y. J. T. and S. C. conceived the ideas and wrote the paper. Y. J. T. synthesized the materials and performed the experiments. W. C. F. help analyze the data. X. T. G., Y. Y. S., and S. T. Z. help edit and polish the paper. H. G. X. supervised the work. H. P. supervised the work and provided the funding. All the authors have approved the final manuscript.

Use of AI statement

None.

References

[1] Cao, L.; Dai, P. C.; Tang, J.; Li, D.; Chen, R. H.; Liu, D. D.; Gu, X.; Li, L. J.; Bando, Y.; Ok, Y. S. et al. Spherical superstructure of boron nitride nanosheets derived from boron-containing metal-organic frameworks. *J. Am. Chem. Soc.* **2020**, *142*, 8755–8762.

[2] Zou, L. L.; Kitta, M.; Hong, J. H.; Suenaga, K.; Tsumori, N.; Liu, Z.; Xu, Q. Fabrication of a spherical superstructure of carbon nanorods. *Adv. Mater.* **2019**, *31*, 1900440.

[3] Wang, H. F.; Chen, L. Y.; Wang, M.; Liu, Z.; Xu, Q. Hollow spherical superstructure of carbon nanosheets for bifunctional oxygen reduction and evolution electrocatalysis. *Nano Lett.* **2021**, *21*, 3640–3648.

[4] Feng, L.; Wang, K. Y.; Yan, T. H.; Zhou, H. C. Seed-mediated evolution of hierarchical metal-organic framework quaternary superstructures. *Chem. Sci.* **2020**, *11*, 1643–1648.

[5] Li, X. R.; Li, Y. P.; Wang, C. L.; Xue, H. G.; Pang, H.; Xu, Q. A 3D hierarchical electrocatalyst: Core–shell Cu@$Cu(OH)_2$ nanorods/MOF octahedra supported on N-doped carbon for oxygen evolution reaction. *Nano Res.* **2023**, *16*, 8012–8017.

[6] Zhao, Z. W.; Duan, L. L.; Zhao, Y. J.; Wang, L. P.; Zhang, J. Y.; Bu, F. X.; Sun, Z. H.; Zhang, T. S.; Liu, M. L.; Chen, H. X. et al. Constructing unique mesoporous carbon superstructures via monomicelle interface confined assembly. *J. Am. Chem. Soc.* **2022**, *144*, 11767–11777.

[7] Shen, Z. Z.; Guo, X. T.; Ding, H. Y.; Yu, D. H.; Chen, Y. H.; Li, N. N.; Zhou, H. J.; Zhang, S. T.; Wu, J.; Pang, H. Construction of ternary Sn/SnO_2/nitrogen-doped carbon superstructures as anodes for advanced lithium-ion batteries. *Nano Res.* **2024**, *17*, 9721–9727.

[8] Zhang, H.; Guo, X. Y.; Wang, X. Noble metal nanoclusters-decorated NiFe layered double hydroxide superstructure as nanoreactors for selective hydrogenation catalysis. *Nanoscale* **2020**, *12*, 17780–17785.

[9] Tang, Y. J.; Zheng, S. S.; Cao, S.; Yang, F. Y.; Guo, X. T.; Zhang, S. T.; Xue, H. G.; Pang, H. Hollow mesoporous carbon nanospheres space-confining ultrathin nanosheets superstructures for efficient capacitive deionization. *J. Colloid Interface Sci.* **2022**, *626*, 1062–1069.

[10] Hou, C. C.; Zou, L. L.; Wang, Y.; Xu, Q. MOF-mediated fabrication of a porous 3D superstructure of carbon nanosheets decorated with ultrafine cobalt phosphide nanoparticles for efficient electrocatalysis and zinc-air batteries. *Angew. Chem., Int. Ed.* **2020**, *59*, 21360–21366.

[11] Song, Y. J.; Song, X. K.; Wang, X. K.; Bai, J. Z.; Cheng, F.; Lin, C.; Wang, X.; Zhang, H.; Sun, J. H.; Zhao, T. J. et al. Two-dimensional metal-organic framework superstructures from ice-templated self-assembly. *J. Am. Chem. Soc.* **2022**, *144*, 17457–17467.

[12] Ding, J. N.; Tang, Y. J.; Zheng, S. S.; Zhang, S. T.; Xue, H. G.; Kong, Q. Q.; Pang, H. The synthesis of MOF derived carbon and its application in water treatment. *Nano Res.* **2022**, *15*, 6793–6818.

[13] Lu, Y. B.; Zhang, G. X.; Zhou, H. J.; Cao, S.; Zhang, Y.; Wang, S. L.; Pang, H. Enhanced active sites and stability in nano-MOFs for electrochemical energy storage through dual regulation by tannic acid. *Angew. Chem., Int. Ed.* **2023**, *62*, e202311075.

[14] Wang, W. H.; Yan, H. W.; Anand, U.; Mirsaidov, U. Visualizing the conversion of metal-organic framework nanoparticles into hollow layered double hydroxide nanocages. *J. Am. Chem. Soc.* **2021**, *143*, 1854–1862.

[15] Zheng, K.; Liao, L. P.; Zhang, Y.; Tan, H.; Liu, J. Q.; Li, C. W.; Jia, D. D. Hierarchical NiCo-LDH core/shell homostructural electrodes with MOF-derived shell for electrochemical energy storage. *J. Colloid Interface Sci.* **2022**, *619*, 75–83.

[16] Liu, C. L.; Feng, W. H.; Bai, Y.; Pang, H. Compositing MXenes with hierarchical ZIF-67/cobalt hydroxide via controllable *in situ* etching for a high-performance supercapacitor. *Inorg. Chem. Front.* **2022**, *9*, 5463–5468.

[17] Li, Z.; Mao, S. D.; Yang, Y.; Sun, Z.; Zhao, R. Controllable synthesis of a hollow core–shell Co-Fe layered double hydroxide derived from Co-MOF and its application in capacitive deionization. *J. Colloid Interface Sci.* **2021**, *585*, 85–94.

[18] Xiao, M. J.; Wu, C.; Zhu, J. W.; Zhang, C. T.; Li, Y.; Lyu, J. H.; Zeng, W. H.; Li, H. W.; Chen, L.; Mu, S. C. *In situ* generated layered NiFe-LDH/MOF heterostructure nanosheet arrays with abundant defects for efficient alkaline and seawater oxidation. *Nano Res.* **2023**, *16*, 8945–8952.

[19] Lei, J. J.; Xiong, Y. C.; Yu, F.; Ma, J. Flexible self-supporting CoFe-LDH/MXene film as a chloride ions storage electrode in capacitive deionization. *Chem. Eng. J.* **2022**, *437*, 135381.

[20] Wang, K.; Liu, Y.; Ding, Z. B.; Chen, Z. Q.; Xu, X. T.; Wang, M.; Lu, T.; Pan, L. K. Chloride pre-intercalated CoFe-layered double hydroxide as chloride ion capturing electrode for capacitive deionization. *Chem. Eng. J.* **2022**, *433*, 133578.

[21] Peng, G. G.; Zhang, Z. H.; Li, H. B. Designing NiFe-metal organic frameworks@NiFe-layered double hydroxide/carbon fiber self-supporting electrode for enhanced capacitive deionization. *Desalination* **2024**, *582*, 117665.

[22] Liu, X. H.; Xu, X. T.; Xuan, X. X.; Xia, W.; Feng, G. L.; Zhang, S. H.; Wu, Z. G.; Zhong, B. H.; Guo, X. D.; Xie, K. Y. et al. Unlocking enhanced capacitive deionization of $NaTi_2(PO_4)_3$/carbon materials by the yolk-shell design. *J. Am. Chem. Soc.* **2023**, *145*, 9242–9253.

[23] Tang, Y. J.; Shi, Y. X.; Su, Y. C.; Cao, S.; Hu, J. L.; Zhou, H. J.; Sun, Y. Y.; Liu, Z.; Zhang, S. T.; Xue, H. G. et al. Enhanced capacitive deionization of hollow mesoporous carbon spheres/MOFs derived nanocomposites by interface-coating and space-encapsulating design. *Adv. Sci.* **2024**, *11*, 2403802.

[24] Xu, H. X.; Zhang, G. Z.; Wang, Y.; Ning, M. Q.; Ouyang, B.; Zhao, Y.; Huang, Y.; Liu, P. B. Size-dependent oxidation-induced phase engineering for MOFs derivatives via spatial confinement strategy toward enhanced microwave absorption. *Nano-Micro Lett.* **2022**, *14*,

102.
[25] Xiong, W. F.; Li, H. F.; You, H. H.; Cao, M. N.; Cao, R. Encapsulating metal organic framework into hollow mesoporous carbon sphere as efficient oxygen bifunctional electrocatalyst. *Natl. Sci. Rev.* **2020**, *7*, 609–619.
[26] Hu, T. T.; Gu, Z.; Williams, G. R.; Strimaite, M.; Zha, J. J.; Zhou, Z.; Zhang, X. C.; Tan, C. L.; Liang, R. Z. Layered double hydroxide-based nanomaterials for biomedical applications. *Chem. Soc. Rev.* **2022**, *51*, 6126–6176.
[27] Zhang, L. Y.; Cai, P. F.; Wei, Z. H.; Liu, T.; Yu, J. G.; Al-Ghamdi, A. A.; Wageh, S. Synthesis of reduced graphene oxide supported nickel-cobalt-layered double hydroxide nanosheets for supercapacitors. *J. Colloid Interface Sci.* **2021**, *588*, 637–645.
[28] Li, C. Y.; Dai, Z. Q.; Liu, W.; Kantichaimongkol, P.; Yu, P. F.; Pattananuwat, P.; Qin, J. Q.; Zhang, X. Y. A self-sacrifice template strategy to synthesize Co-LDH/MXene for lithium-ion batteries. *Chem. Commun.* **2021**, *57*, 11378–11381.
[29] Li, N.; Yang, T.; Huang, L. J.; Jiang, H.; Xiao, J. X.; Ma, X. Y.; Lou, H.; Xie, C.; Yang, Y. H. Interfacial coupling engineering boosting electrocatalytic performance of CoFe layered double hydroxide assembled on N-doped porous carbon nanosheets for water splitting and flexible zinc-air batteries. *ACS Appl. Mater. Interfaces* **2023**, *15*, 52530–52541.
[30] Guan, X. H.; Huang, M. H.; Yang, L.; Wang, G. S.; Guan, X. Facial design and synthesis of CoS_x/Ni-Co LDH nanocages with rhombic dodecahedral structure for high-performance asymmetric supercapacitors. *Chem. Eng. J.* **2019**, *372*, 151–162.
[31] Cao, S.; Lu, Y. B.; Tang, Y. J.; Sun, Y. Y.; Zhou, H. J.; Zhang, G. X.; Lin, X. Y.; Pang, H. Constructing ion-transport blockchain by polypyrrole to link CoTi-ZIF-9 derived carbon materials for high-performance seawater desalination. *J. Colloid Interface Sci.* **2024**, *654*, 466–475.
[32] Zhang, W. X.; Arramel, A.; Wong, P. K. J.; Zhang, L.; Zheng, J. Z.; Zhang, W.; Zhang, H.; Yan, X.; Qi, J. W.; Li, J. S. Core–shell hybrid zeolitic imidazolate framework-derived hierarchical carbon for capacitive deionization. *J. Mater. Chem. A* **2020**, *8*, 14653–14660.
[33] Ding, M.; Du, F. H.; Liu, B.; Leong, Z. Y.; Guo, L.; Chen, F. M.; Baji, A.; Yang, H. Y. Rod-like nitrogen-doped carbon hollow shells for enhanced capacitive deionization. *FlatChem* **2018**, *7*, 10–17.
[34] Tang, Y. J.; Ding, J. N.; Zhou, W. X.; Cao, S.; Yang, F. Y.; Sun, Y. Y.; Zhang, S. T.; Xue, H. G.; Pang, H. Design of uniform hollow carbon nanoarchitectures: Different capacitive deionization between the hollow shell thickness and cavity size. *Adv. Sci.* **2023**, *10*, 2206960.
[35] Meng, F. Y.; Ding, Z. B.; Xu, X. T.; Liu, Y.; Lu, T.; Pan, L. K. Metal organic framework-derived nitrogen-doped porous carbon sustained Prussian blue analogues for efficient and fast hybrid capacitive deionization. *Sep. Purif. Technol.* **2023**, *317*, 123899.
[36] Li, Y.; Yong, T. Z.; Qi, J. W.; Wu, J. S.; Lin, R. Y.; Chen, Z. H.; Li, J. S. Enhancing the electronic and ionic transport of flow-electrode capacitive deionization by hollow mesoporous carbon nanospheres. *Desalination* **2023**, *550*, 116381.
[37] Li, Y.; Qi, J. W.; Li, J. S.; Shen, J. M.; Liu, Y. X.; Sun, X. Y.; Shen, J. Y.; Han, W. Q.; Wang, L. J. Nitrogen-doped hollow mesoporous carbon spheres for efficient water desalination by capacitive deionization. *ACS Sustain. Chem. Eng.* **2017**, *5*, 6635–6644.
[38] Du, J. X.; Xing, W. L.; Yu, J. Q.; Feng, J.; Tang, L.; Tang, W. W. Synergistic effect of intercalation and EDLC electrosorption of 2D/3D interconnected architectures to boost capacitive deionization for water desalination via $MoSe_2$/mesoporous carbon hollow spheres. *Water Res.* **2023**, *235*, 119831.
[39] Wei, D.; Cao, Y. Y.; Yan, L. J.; Gang, H. Y.; Wu, B. C.; Ouyang, B. X.; Chen, P.; Jiang, Y. X.; Wang, H. Y. Enhanced pseudo-capacitance process in nanoarchitectural layered double hydroxide nanoarrays hollow nanocages for improved capacitive deionization performance. *ACS Appl. Mater. Interfaces* **2023**, *15*, 24427–24436.
[40] Wang, W. Y.; Wang, Y. Y.; Wang, X. Q.; Jiang, B. L.; Song, H. Engineering hollow core–shell N-C@Co/N-C catalysts with bits of Ni doping used as efficient electrocatalysts in microbial fuel cells. *ACS Appl. Mater. Interfaces* **2022**, *14*, 41912–41923.
[41] Gao, M.; Li, J. X.; Wang, Z.; Yang, Z. Q.; Chen, Y.; Deng, W. Y.; Liang, W. C.; Ao, T. Q.; Chen, W. Q. Hierarchical nickel cobaltite nanoneedle arrays armored flexible electrospinning carbon nanofibers membrane for electrochemical deionization. *Sep. Purif. Technol.* **2024**, *328*, 125084.
[42] Xing, Z. Y.; Xuan, X. X.; Hu, H. Y.; Li, M. H.; Gao, H. M.; Alowasheeir, A.; Jiang, D.; Zhu, L. Y.; Li, Z. T.; Kang, Y. Q. et al. Particle size optimization of metal-organic frameworks for superior capacitive deionization in oxygenated saline water. *Chem. Commun.* **2023**, *59*, 4515–4518.
[43] Guo, J. R.; Xu, X. T.; Hill, J. P.; Wang, L. P.; Dang, J. J.; Kang, Y. Q.; Li, Y. L.; Guan, W. S.; Yamauchi, Y. Graphene-carbon 2D heterostructures with hierarchically-porous P,N-doped layered architecture for capacitive deionization. *Chem. Sci.* **2021**, *12*, 10334–10340.
[44] Xu, Y. S.; Xiang, S. H.; Mao, H. J.; Zhou, H. J.; Wang, G. Z.; Zhang, H. M.; Zhao, H. J. Pseudocapacitive desalination via valence engineering with spindle-like manganese oxide/carbon composites. *Nano Res.* **2021**, *14*, 4878–4884.
[45] Zhang, H.; Zhang, W. X.; Shen, J. M.; Li, Y.; Yan, X.; Qi, J. W.; Sun, X. Y.; Shen, J. Y.; Han, W. Q.; Wang, L. J. et al. Ag-doped hollow ZIFs-derived nanoporous carbon for efficient hybrid capacitive deionization. *Desalination* **2020**, *473*, 114173.
[46] Zhang, B.; Yi, Q. Y.; Qu, W. Q.; Zhang, K.; Lu, Q.; Yan, T. T.; Zhang, D. S. Titanium carbon oxide flakes with tunable interlayer spacing for efficient capacitive deionization. *Adv. Funct. Mater.* **2024**, *34*, 2401332.
[47] Shen, G. Z.; Guo, Z. X.; Zhang, L.; Ma, Q. H.; Xiao, C. Y.; Qin, C. J.; Chong, H. L. H.; Moh, P. Y.; Liu, Y.; Yuan, X. Rational design of sea urchin-like FeOOH anchored hollow carbon spheres as chloride-insertion electrodes for efficient faradic capacitive deionization. *Sep. Purif. Technol.* **2024**, *335*, 126034.
[48] Obisanya, A. A.; Ma, L.; Liu, J. K.; Yang, T. S.; Ren, Z. B.; Tan, X. Y.; Gao, F. M.; Wang, J. R. Multiscale scrutinizing ion storage kinetics in hollow Ni-Mn prussian blue analogues for enhanced capacitive deionization. *Adv. Funct. Mater.* **2024**, *34*, 2404591.
[49] Guo, J. B.; Li, L.; Luo, J.; Gong, W. B.; Pan, R.; He, B.; Xu, S. H.; Liu, M. N.; Wang, Y. J.; Zhang, B. H. et al. Polypyrrole-assisted nitrogen doping strategy to boost vanadium dioxide performance for wearable nonpolarity supercapacitor and aqueous Zinc-Ion battery. *Adv. Energy Mater.* **2022**, *12*, 2201481.